03

Swirling MHD-flow in a closed channel with a circular cross-section

© I.Y. Mitropolit,[1] E. Golbraikh,[2] I.V. Kolesnichenko[1]

[1]Institute of Continuous Media Mechanics, Ural Branch, Russian Academy of Sciences,
614013 Perm, Russia
[2]Ben Gurion University of the Negev,
8410501 Beer Sheva, Israel
e-mail: mitropolit.i@icmm.ru

Received June 6, 2025
Revised September 26, 2025
Accepted September 29, 2025

In this article, the hydrodynamic characteristics of the liquid metal flow created inside a closed channel with a circular cross-section by the combined action of travelling and rotating magnetic fields of different values of the corresponding force parameters are investigated using numerical modeling. The dependences of the pressure drop, flow rate, flow energy and other quantities on the value of the rotating magnetic field force parameter are obtained.The influence of the intensity of the swirling of the liquid metal realized by the rotating magnetic field on the characteristics of the flow created by the travelling magnetic field is assessed. The values of the force parameter of the rotating magnetic field are obtained, at which it is possible to achieve an increase in the pressure drop between the channel inlet and outlet due to the swirling of the flow, and assumptions are made about the physical causes of this effect. The influence of structural elements in the considered channel configuration on the flow properties is estimated.

Keywords: magnetohydrodynamics, numerical modeling, travelling magnetic field, rotating magnetic field.

DOI: 10.61011/TP.2026.02.62873.142-25

Introduction

Generation of magnetohydrodynamic (MHD) liquid metal flows in circular cross-section channels is an important process in modern iron and steel, and power engineering technologies. In steel and iron industry, liquid metal is transported from melting furnaces to foundries [1]. In power engineering, liquid metal is used as coolant for fast neutron nuclear power plants [2]. Besides motor pumps, electromagnetic pumps are widely used to create transit flow. Pumping action in these pumps is initiated by contactless electromagnetic force generation in liquid metal [3]. By the method of current generation in metal, pumps are classified into conduction and induction pumps [4,5]. Cylindrical line induction pump (CLIP) appeared to be the most popular one [4]. Such pumps, apart from extensive use in nuclear industry where specifically high requirements for equipment performance are established [6], are also widely used in test bench studies [7]. Some features of pump operation may serve as the basis for measurement procedures [8,9]. This type of pumps is also used in steel and iron industry [10,11]. An adaptable design of such pumps capable of solving most existing problems is currently not available, which is the reason for continuous exploratory research [12].

CLIP is a set of short toroidal solenoid windings „put“ on the channel and connected to power supply in such a way as to induce travelling magnetic field (TMF) in metal. To isolate magnetic induction, an external yoke core is used, and a cylindrical ferromagnetic insert is placed into the channel, thus, turning the cylindrical channel into a slit one [4,6,13]. It is the inductor and channel design that provides the highest CLIP performance. Typical size of the pump is about 1 m, and the size of a slit gap, via which liquid metal flows, is from 3 mm to 10 mm. Typical melt velocity in the channel varies from several centimeters per second to several meters per second.

However, there are several issues with CLIP operation. The first of them is associated with the fact that there must be an electromagnetic pump mounted on the existing cylindrical channel without dismantling. In this case, there is no passive core with a ferromagnetic material in the channel, and the channel is cylindrical, rather than slit, i.e. the above-mentioned CLIP design is not suitable because the force will be generated near the channel wall. This in turn will induce reverse flow through the central part of the channel and considerably reduce the pump performance. It is necessary to modify the pump design to ensure the most homogeneous force profile across the channel. The second problem is in the absence of azimuthal force component and, consequently, of azimuthal velocity in the CLIP channel. Although the pump is manufactured with utmost care, it is very difficult to maintain a uniform gap. This leads to nonuniform velocity in the channel, occurrence of dead zones where contaminations or gas inclusions are formed, and hot spots, which reduce performance and cause flow rate fluctuations.

These problems may be solved by means of a demountable inductor, which is discussed in this work and whose equivalent is described in [14]. The inductor is used to generate both travelling and rotating magnetic fields (RMF)

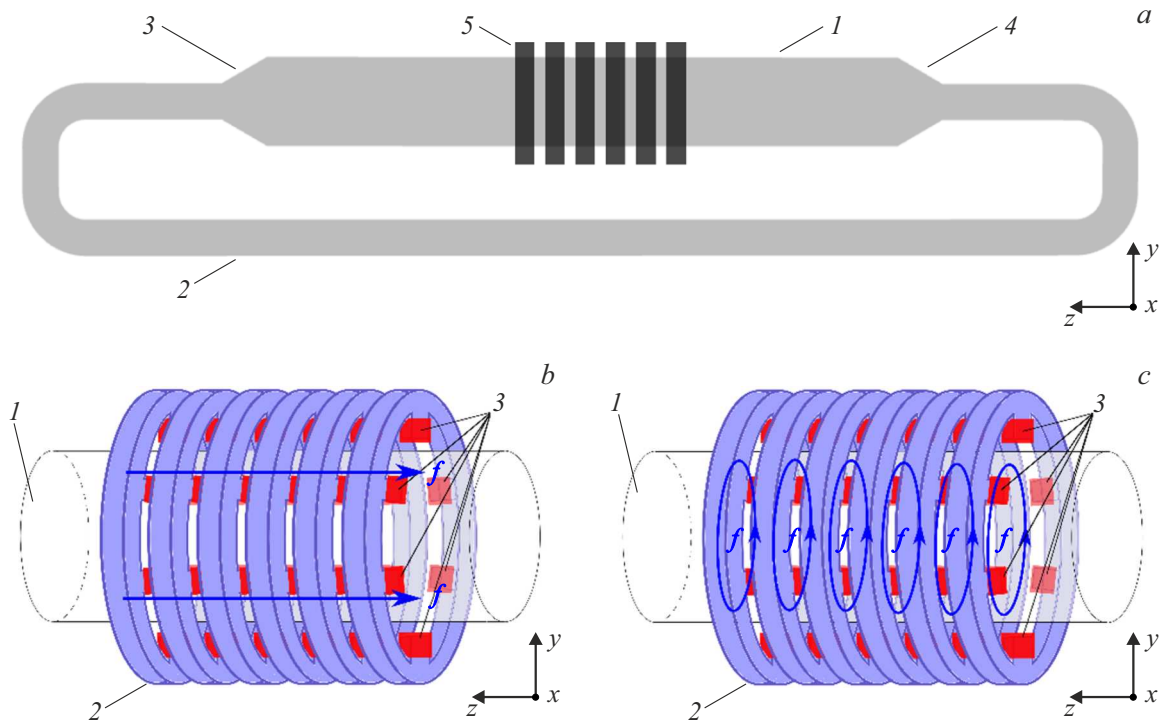

Figure 1. *a* — simulated domain in the *zy* plane: *1* — main cylindrical channel, *2* — closing channel, *3* — diffuser, *4* — confuser, *5* — travelling or rotating field inductor; *b* — TMF inductor diagram: *1* — cylindrical channel, *2* — six-piece magnetic field inductor, *3* — generating coils; *c* — RMF inductor diagram: *1* — cylindrical channel, *2* — six-piece magnetic field inductor, *3* — generating coils.

with online control of each of them. Impact of RMF created by an inductor identical design on liquid metal flow properties was explored in [15]. Its high efficiency and ease of rotating flow generation are demonstrated. In [13], focus was made on the impact of only inductor-generated TMF on the flow. An effective flow rate calculation method was proposed and is used in this work. It was found that the additional inserted channel improves integral flow characteristics, in particular, due to reducing reverse flow intensity. Nevertheless, even when there is no insert in the empty channel, TMF generates transit flow with adequate flow rate. Joint action of TMF and RMF is extensively studied in terms of improvement of liquid metal alloy mixing processes. Many papers [16–19] show the efficiency of this approach, however, the vast majority of them discuss liquid metal flow in limited cylindrical cells, rather than in channels. Effect of magnetic fields on liquid metal was also explored, for example, in terms of separation problems [20]. However, transit flow in the channel was not included in these problems.

This work investigates the properties of liquid metal flow induced in the closed circular cross-section channel by the joint action of TMF and RMF. The channel has no any inserts. The electromagnetic force is produced in a contactless manner by an external inductor. Inductor length, which defines the size of the field of action of the electromagnetic forces, is much shorter than the channel length. This setting features coincident fields of action of TMF and RMF, while the intensity of these magnetic fields can be set separately. TMF induces the electromagnetic force that is predominantly directed along the channel axis and generates the transit flow. RMF induces the electromagnetic force that is predominantly directed in azimuth and generates flow rotation. The aim of this work is to use computational simulation for evaluating the effect of RMF-induced liquid metal swirling intensity on the properties of TMF-induced transit flow.

1. Mathematical model

Processes of formation and evolution of swirling liquid metal flows induced by RMF and TMF were studied in a domain consisting of a circular cross-section closed-loop channel. The channel can be nominally divided into subdomains as shown in Figure 1, *a*: main cylindrical channel *1* with radius R, closing channel *2* with radius r, that has four bend sections, diffuser *3*, and confuser *4*. Inductor *5*, generating travelling and rotating magnetic fields, is placed around the main channel. Figure 1, *b*, *c* shows schematic diagrams of TMF and RMF inductors. In the given model, each of them is a set of six ring sections consisting of ferromagnetic core *2* and six generating coils (solenoid windings) *3* put on the core. TMF and RMF inductors have no structural difference and the type of field generated by the inductor is defined only by the generating

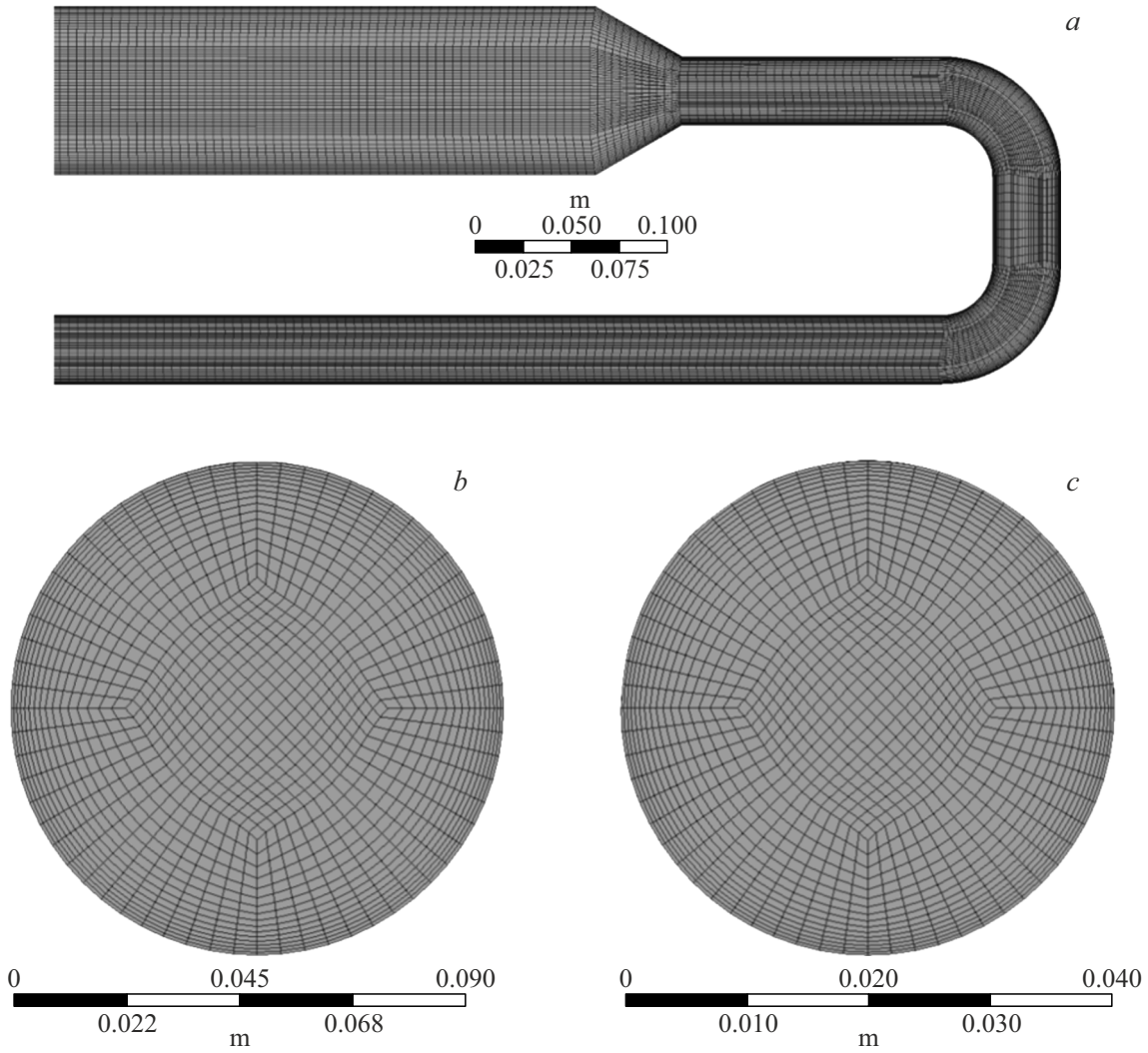

Figure 2. *a* — computational mesh in the longitudinal midsection of the channel (zy plane); *b*, *c* — computational mesh in the transverse cross-section of the channel (xy plane): *b* — main channel, *c* — closing channel.

coil connection circuits. Configuration of this inductor is described in more detail in [14,15].

Closed configuration of the given channel was chosen for a number of reasons. Firstly, this solves the issue of setting boundary conditions, which occurs in such problems. The issue is in that it is impossible to set the differential pressure or periodic velocity inlet and outlet boundary conditions because the differential pressure and flow rate, or rather, their dependences on the force parameter and magnetic field configuration are the quantities investigated in this problem. Secondly, flow in a closed channel is from physical standpoint closer to liquid metal flow in a pipe in real processes or experimental studies. In other words, the influence of structural elements such as, for example, channel bends on hydrodynamic processes in liquid metals can be additionally investigated. To reduce computational efforts by reducing the volume of computational domain, the closing channel was set to a smaller radius than the main channel. Hence, it is necessary to introduce a diffuser and confuser into the channel. These are structural elements that are widely used in fluid dynamics and whose effect on the processes being investigated will be also important to be estimated.

Mathematical model is built on the basis of magnetic hydrodynamics (MHD) equations, which describe the interaction between flowing conducting fluids and electric and magnetic fields. A key parameter, which defines the mutual influence of flow and magnetic field on each other, is the magnetic Reynolds number $R_{em} = \sigma\mu\mu_0 UL$, where σ is the liquid conductivity, μ is the liquid permeability, μ_0 is the vacuum permeability, U is the overall mean axial fluid velocity, L is the typical length. Preliminary estimates have shown that within the processes being investigated in this problem $R_{em} \sim 0.17$, meaning that transfer of magnetic field by liquid metal flow is quite small. Magnetic induction B was of the order from 10^{-4} to 10^{-2}, and the Hartmann number (Ha), defining the ratio of magnetic force to viscous force, was < 3. The above-mentioned estimates have shown

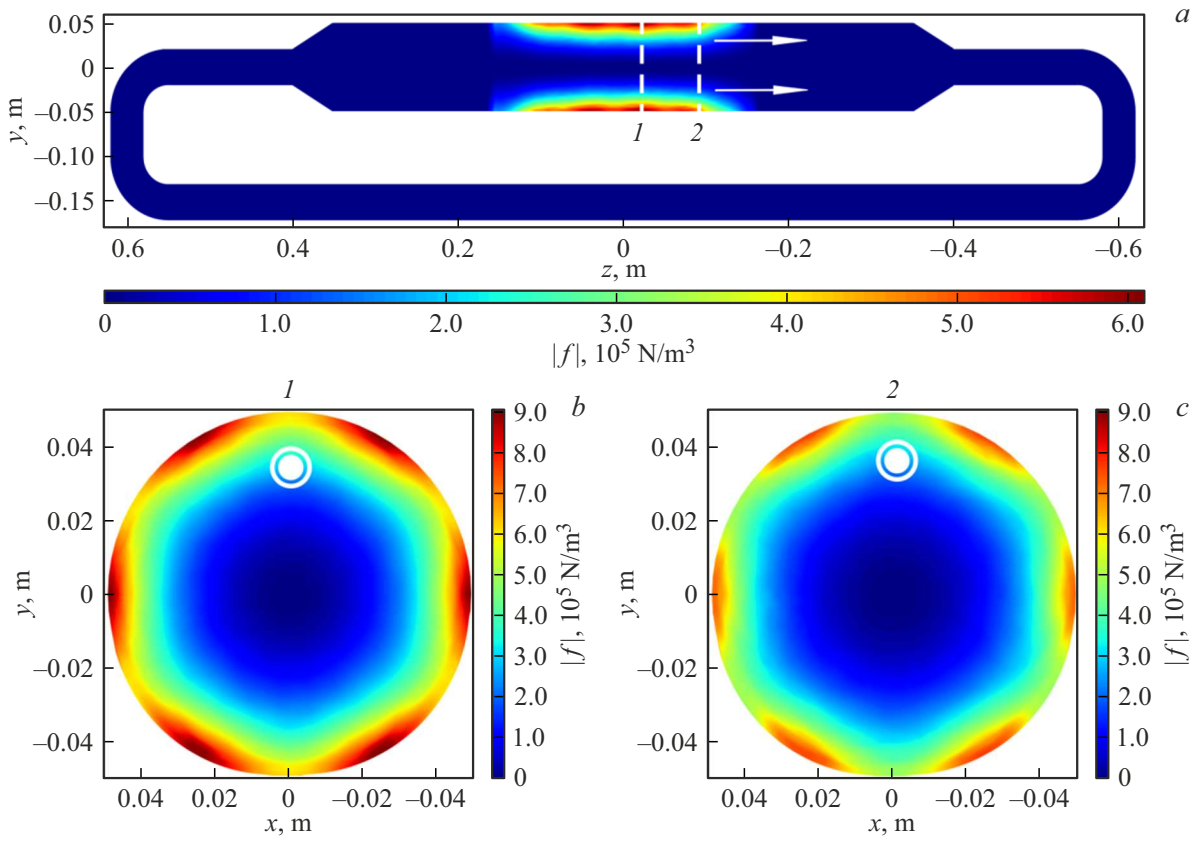

Figure 3. Field of the magnitude of TMF-induced volume electromagnetic force: *a* — in the *zy*plane, *1*, *2* — domains where the magnitude of force was additionally explored in the *xy* plane, arrows show the force direction; *b* — in the *xy* plane, *1* — domain where forces were read, the force direction (at us) is marked by a dot; *c* — in the *xy* plane, *2* — domain where forces were read, the force direction (at us) is marked by a dot.

that electrodynamic and hydrodynamic problems could be solved separately, i.e. the system of MHD equations could be used in electrodynamic approximation.

Electrodynamic subproblem was solved using the system of Maxwell's equations without displacement current and supplemented by Ohm's law:

$$\nabla \times \mathbf{H} = \mathbf{j}_c, \tag{1}$$

$$\frac{\partial B}{\partial t} = -\nabla \times \mathbf{E}, \tag{2}$$

$$\nabla \cdot \mathbf{E} = 0, \quad \nabla \cdot \mathbf{B} = 0, \tag{3}$$

$$\mathbf{j} = \sigma \mathbf{E}, \tag{4}$$

where $\mathbf{H}$ is the magnetic field strength, $\mathbf{j}_c$ is the current density on coils, $\mathbf{B}$ is the magnetic induction, t is the time, $\mathbf{E}$ is the electric field strength, $\mathbf{j}$ is the vortex current.

It is important to note that the vortex current in the core and on coils is not included in this problem. Electromagnetic force $\mathbf{f}$ driving the metal is

$$\mathbf{f} = \mathbf{j} \times \mathbf{B}. \tag{5}$$

Equality to zero of the vortex current density vector component normal to the channel boundary (outer wall) is taken as a boundary condition.

Liquid metal flow in the channel induced by the action of electromagnetic force is described by the Reynolds-averaged Navier–Stokes equations closed according to Boussinesq's hypothesis, which introduces turbulent viscosity, and by the continuity equation:

$$\frac{\partial \mathbf{v}}{\partial t} + \mathbf{v} \cdot \mathbf{v} = \frac{\nabla P}{\rho} + \nabla \cdot [(\nu + \nu_t)(\nabla \mathbf{v} + (\nabla \mathbf{v})^T)] + \frac{\mathbf{f}}{\rho}, \tag{6}$$

$$\nabla \cdot \mathbf{v} = 0. \tag{7}$$

In (6), (7), $\mathbf{v}$ is the liquid velocity, ν is the kinematic viscosity, ν_t is the turbulent viscosity, ρ is the liquid metal density, P is the pressure.

No-slip conditions on the channel walls were set as a boundary condition: $\mathbf{v} = 0$.

Velocity $\mathbf{v}$ and pressure P at the initial time were taken equal to zero.

It has been noted earlier that liquid metal flow is induced by the electromagnetic force, moreover, for the TMF and RMF cases, direction of this force will differ significantly. In both cases, the action of force is localized near the channel walls, however, TMF induces the force acting in the axial direction (Figure 1, *b*), and RMF induces the force acting in the azimuthal direction (Figure 1, *c*). The Taylor number is

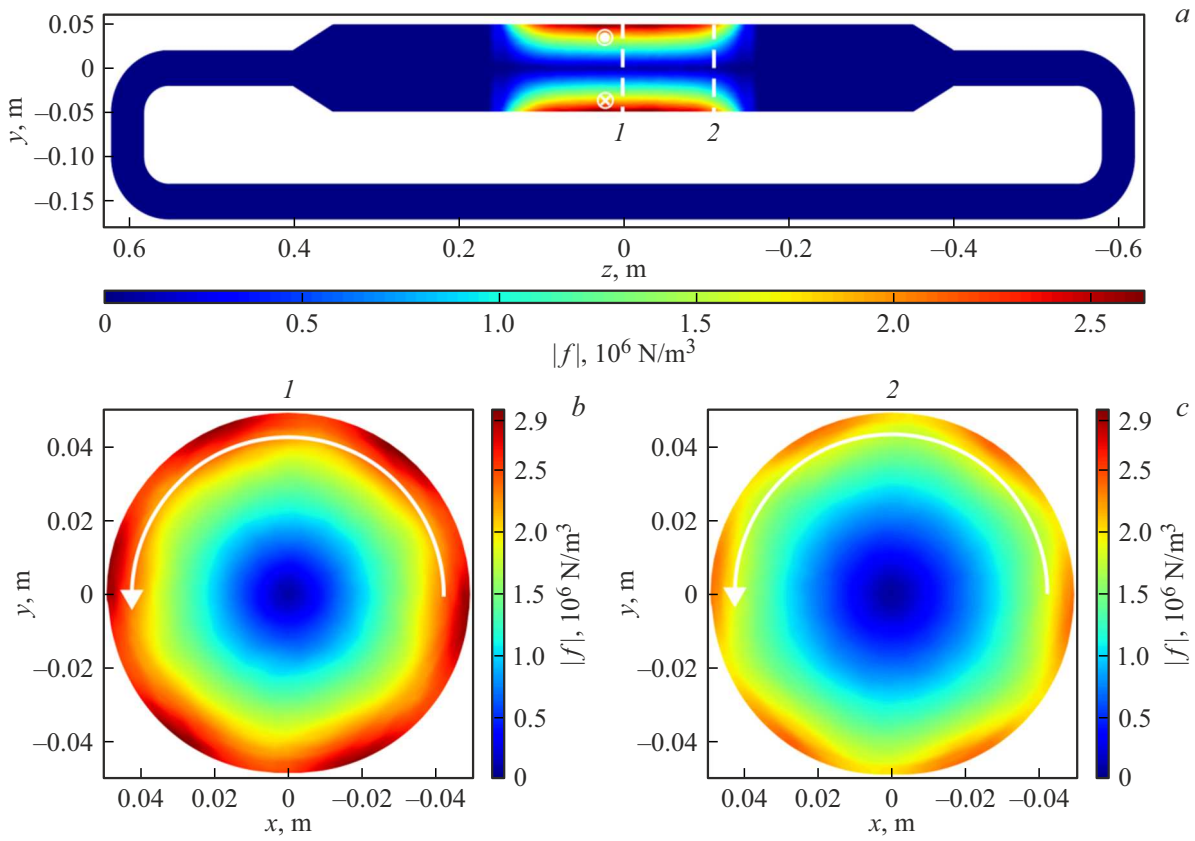

Figure 4. Field of the magnitude of RMF-induced volume electromagnetic force: *a* — in the *zy*plane, *1*, *2* — domains where the magnitude of force was additionally explored in the *xy* plane, a dot and cross show the force direction (at us and from us, respectively); *b* — in the *xy* plane, *1* — domain where forces were read, arrow shows the force direction; *c* — in the *xy* plane, *2* — domain where forces were read, arrow shows the force direction.

used as a dimensionless parameter defining the intensity of electromagnetic force generated by the RMF inductor [21]:

$$Ta_R = \frac{\sigma \omega_R B_R^2 R^4}{2\rho\nu^2},$$

where ω_R is the angular frequency of RMF, B_R is the magnetic induction of RMF, R is the channel radius, ρ and ν is the fluid density and kinematic viscosity. Taylor analogy was used as a TMF force parameter [21,22]:

$$Ta_T = \frac{\sigma \omega_T k_T B_T^2 R^5}{4\rho\nu^2},$$

where ω_T is the angular frequency of TMF, B_T is the magnetic induction of TMF, k_T is the wave number of TMF.

We introduce a dimensionless parameter, which will define the joint effect of TMF and RMF on the conducting fluid:

$$\gamma = \frac{Ta_R}{Ta_T} = \frac{2\omega_R B_R^2}{\omega_T k_T B_T^2 R}.$$

Calculations were performed for a gallium alloy, $Ga_{86.3}Zn_{10.8}Sn_{2.9}$, which was chosen from considerations of comparing simulation results with results of experiment, which is to be carried out in future. The alloy has the following properties at room temperature: $\rho = 6150\,\text{kg/m}^3$, $\nu = 2.9 \cdot 10^{-7}\,\text{m}^2/\text{s}$, $\sigma = 2.6 \cdot 10^6\,\text{S/m}$. The channel, where the alloy flow was created, had the following geometric characteristics: diameter of the main channel $D = 0.098\,\text{m}$ and length of the main channel $l = 0.7\,\text{m}$, diameter of the closing channel $d = 0.04\,\text{m}$.

Electromagnetic parameters of the processes being investigated were determined in ANSYS EMAG. Electromagnetic subproblem solution domain was divided into subdomains: 2 mm stainless steel channel filled with liquid metal, inductor, and air. Current on coils was the control parameter. Permeability of all subdomains was set to 1, i.e. there was no permeability variation in transition between domains. Current short-circuiting to the channel wall is insignificant due to the small wall thickness and stainless steel conductivity, which is by orders of magnitude lower than gallium alloy conductivity. Electrodynamic simulation involved the calculation of vortex electric and magnetic fields, current density and electromagnetic force. The calculation used a block-structured grid with the following parameters: grid step for the liquid metal domain, inductor and channel domain and air domain was set to 0.004 m, 0.01 m, and 0.01 – 0.02 m, respectively. The grid is not

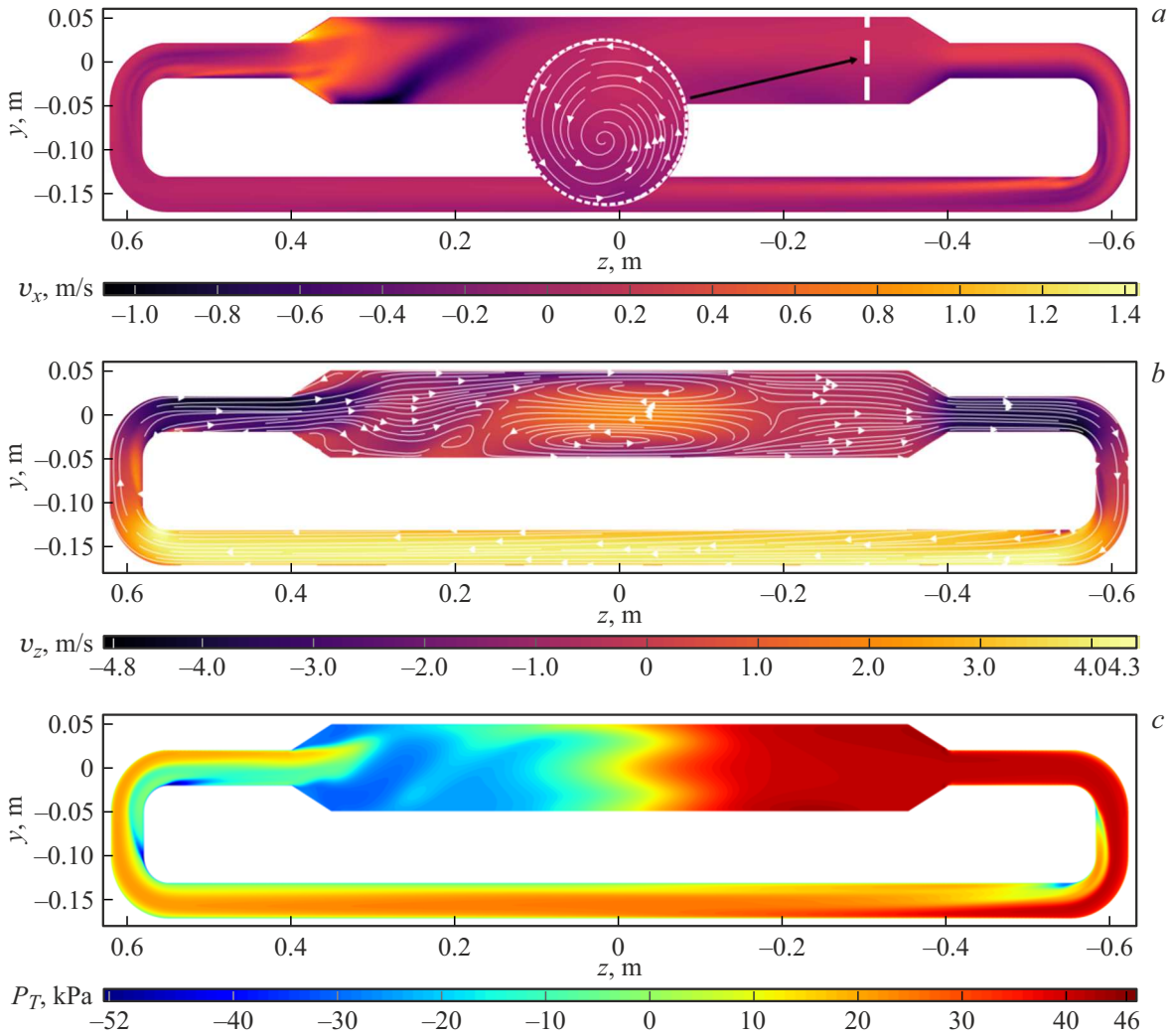

Figure 5. *a* — fields of velocity component vx in the zy plane and xy plane (round inset); *b* — fields of velocity component vz; *c* — fields of P_T in the zy plane at $\gamma = 10^{-3}$.

illustrated in this work due to visualization complexity in ANSYS EMAG.

After determining the electrodynamic parameters, electromagnetic and hydrodynamic subproblems were coupled for the reasons of solving the system of equations in electrodynamic approximation. Coupling was performed by transferring the calculated electromagnetic force components from the electrodynamic subproblem grid to the hydrodynamic subproblem grid using third-party software. Electromagnetic force field derived from the electromagnetic subproblem solution was considered to be time invariant when solving the hydrodynamic subproblem. Hydrodynamic subproblem was solved as a nonstationary steady-state problem where achievement of steady-state flow energy was used as the criterion of flow steady state. Time step was 0.1 s. Hydrodynamic parameters of the given processes were calculated using the finite volume method in ANSYS Fluent. Figure 2 shows the fragments of the computational grid used for solving the hydrodynamic subproblem in different sections. Due to channel and grid symmetry, Figure 2, *a* shows only the right-hand part of the longitudinal midsection (by the zy plane). A block-structured grid was built, a grid step along the channel was 0.005 m, across the channels was ~ 0.0025 m, a grid step across the closing channel was ~ 0.0013 m, minimum cell volume was $9.9 \cdot 10^{-10}\,\mathrm{m}^3$, maximum cell volume was $4.3 \cdot 10^{-8}\,\mathrm{m}^3$. Grid clustering to the channel wall was used: from ~ 0.0025 m to ~ 0.00055 m in the main channel and from ~ 0.0013 m to ~ 0.00025 m in the closing channel. The number of grid elements was $\sim 7 \cdot 10^5$.

Magnetic induction of the corresponding field was varied by varying the magnitude of current on coils. Magnetic induction of TMF in this work was invariant and equal to $B_T = 8.9 \cdot 10^{-3}$ T, and magnetic inductions of RMF were varied within $B_R \in [4.7 \cdot 10^{-4}, 1.49 \cdot 10^{-2}]$ T, while with invariant values $\omega_T = \omega_R = 2\pi \cdot 50$ Hz, $k_T = 114$, $R = 0.049$ m; owing to varying B_R within the specified

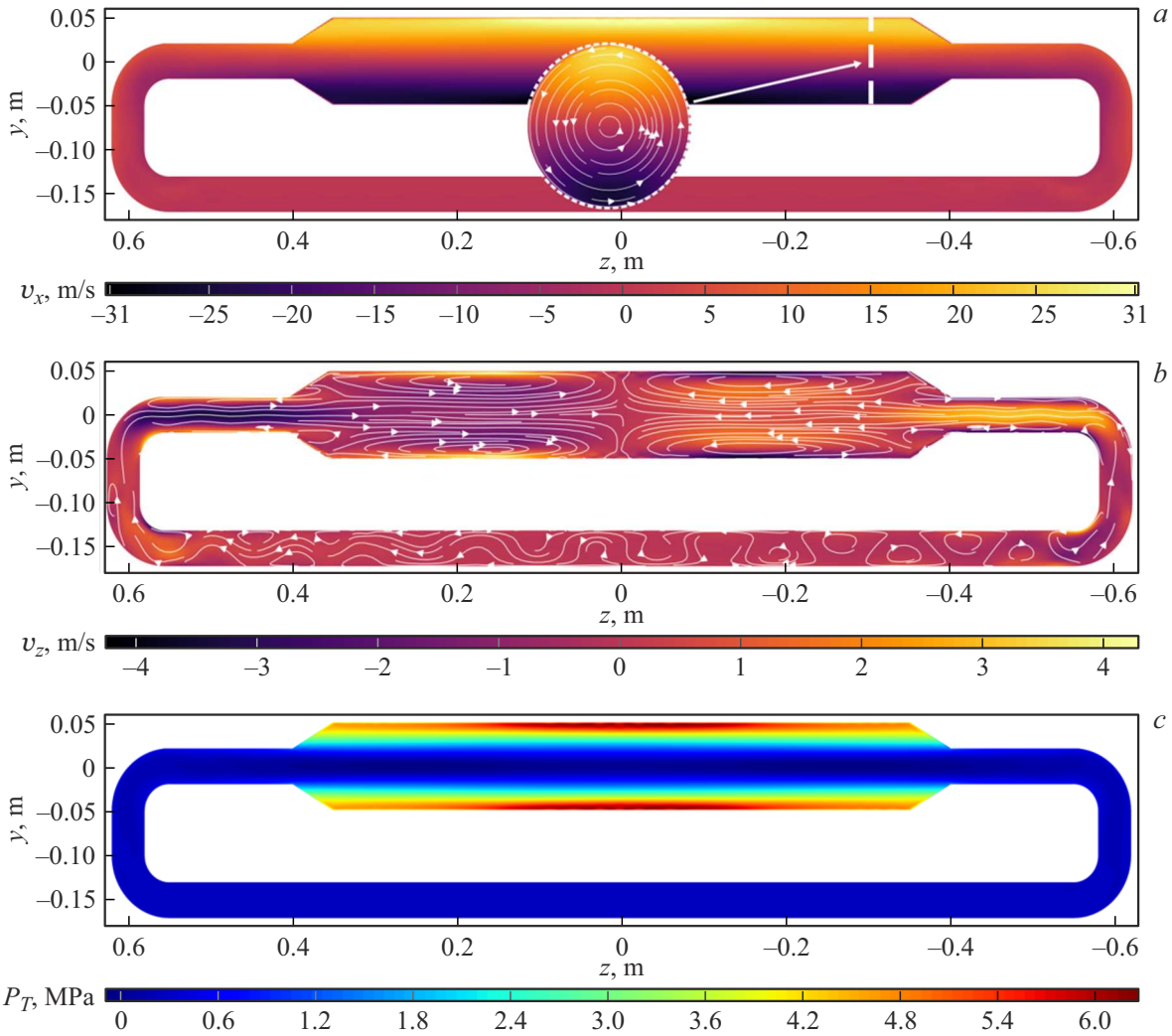

Figure 6. *a* — fields of velocity component vx in the zy plane and xy plane (round inset); *b* — fields of velocity component vz; *c* — fields of P_T in the zy plane at $\gamma = 1$.

range, the dimensionless parameter $Ta_R \in [10^6, 10^9]$. Finally, with fixed $Ta_T = 10^9$, the joint action parameter $\gamma \in [10^{-3}, 1]$.

Preliminary estimates have shown sufficiently high hydrodynamic Reynolds numbers ($\mathrm{Re} > 2.5 \cdot 10^5$), therefore, for the purpose of solution, flow turbulence was considered within the SST model [23,24]. Mathematical computational model for electromagnetic properties and hydrodynamic processes was verified using the experimental results obtained and described in [8,15,25].

2. Results

Consider the values of electromagnetic force induced in the conducting fluid exposed to a variable magnetic field. These values were calculated during solution of the electromagnetic subproblem in ANSYS EMAG for $Ta_T = 10^9$ and $Ta_R = 10^9$. Figures 3 and 4 show the fields of the magnitude of electromagnetic force f in the closed-loop circular cross-section channel under the action of TMF and RMF in the zy and zy planes. Note that longitudinal component of the force f_z generated by RMF is close to zero, therefore the component was not used for magnitude calculation.

Figure 3, *a* shows that f is at its maximum near the channel walls and drops to the channel axis. The force profile shape in this case is caused by the inductor shape: the profile has six peaks equal to the number of inductor rings, while it can be seen that in the axial (longitudinal) direction the force decreases with distance from the center (of inductor, but not of the channel), i.e. the farther the ring is from the center of inductor the weaker induced electromagnetic force is. This pattern is clearly seen in Figure 3, *b*, *c*, where forces are shown in the transverse channel cross-section at different distances from the center of inductor. For better illustration of force weakening, the fields of the magnitudes of force in Figure 3, *b*, *c* were plotted on the same scales. These figures can be also

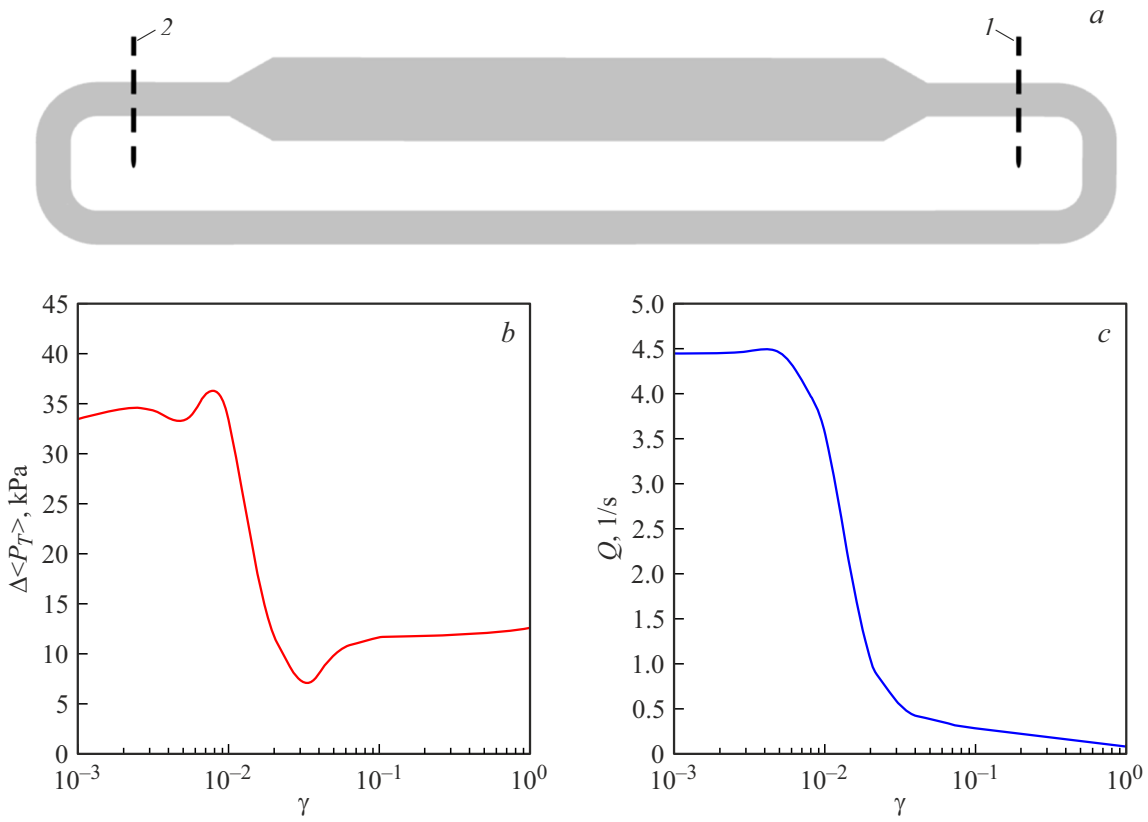

Figure 7. *a* — channel section: *1* — domain where channel outlet $\langle P_T \rangle$ was read, *2* — domain where channel inlet $\langle P_T \rangle$ was read; *b* — differential pressure $\Delta\langle P_T \rangle$ between the main channel inlet and outlet vs. γ; *c* — liquid flow rate Q vs. γ.

used to evaluate the nonuniformity of force action in the azimuthal (circumferential) direction: six domains equal to the number of coils placed on the same inductor ring, where the force is maximum, are clearly seen. Arrows in the figures show the force directions and, accordingly, the main liquid flow direction in the channel. In this case TMF induces transit flow in the main channel and closing channel in inverse direction with respect to the z axis.

High nonuniformity of force distribution in the axial direction is observed only for TMF, and Figure 4, *a* shows that the profile of the magnitude of f generated by RMF has a smoother shape, and in the radial direction the force decreases slower than in the RMF case. Figure 3, *b*, *c* makes it possible to estimate a decrease in the electromagnetic force with distance from the center of inductor as well as nonuniformity of the force in the azimuthal direction, which is less pronounced in this case than in the TMF case. The force shown in Figure 4 will in turn create rotating flow in the channel in direction marked by a dot, cross and arrows in Figure 4.

To estimate hydrodynamic properties of flows induced by the joint action of TMF and RMF on conducting fluid, numerical experiments were carried out. TMF and RMF were applied simultaneously to the liquid metal volume contained in the channel (Figure 1, *a*), and γ varied from 10^{-3} to 1. Figures 5 and 6 show the fields of velocity components v_x, v_z and total pressure PT in the channel for minimum and maximum values of γ. To illustrate the structure of flows in longitudinal and transverse cross-section, streamlines are drawn in the figures of velocity component fields. Round insets in Figure 5, *a* and Figure 6, *a* show velocity component fields v_x on sections formed by the x_y plane in domains marked by white dashed lines. Note that the insets themselves are located in places, where the displayed field in the z_y plane has a homogeneous structure, and don't hide important information. Hereinafter results are shown for the total pressure P_T, i.e. the sum of static and dynamic pressures. It is important that the results shown below refer to the steady-state flow.

In the first case when $\gamma = 10^{-3}$, the axial flow velocity component prevails over the component orthogonal to the section. This is clearly seen in Figure 5, *a* where v_x is close to zero in the most of the channel, though, as shown in the inset, there is a well-defined structure of slowly rotating flow. While the axial component (Figure 5, *b*) in some areas reaches almost 5 m/s. In Figure 5, *b*, there is also a picture of reverse flow induced in the center, which is typical of cylindrical channels and associated with the fact that the electromagnetic force is concentrated near the channel walls. This flow considerably reduces the main flow velocity, which has been shown in [13], and, to a great extent due to interaction with the main flow, the transit flow coming from

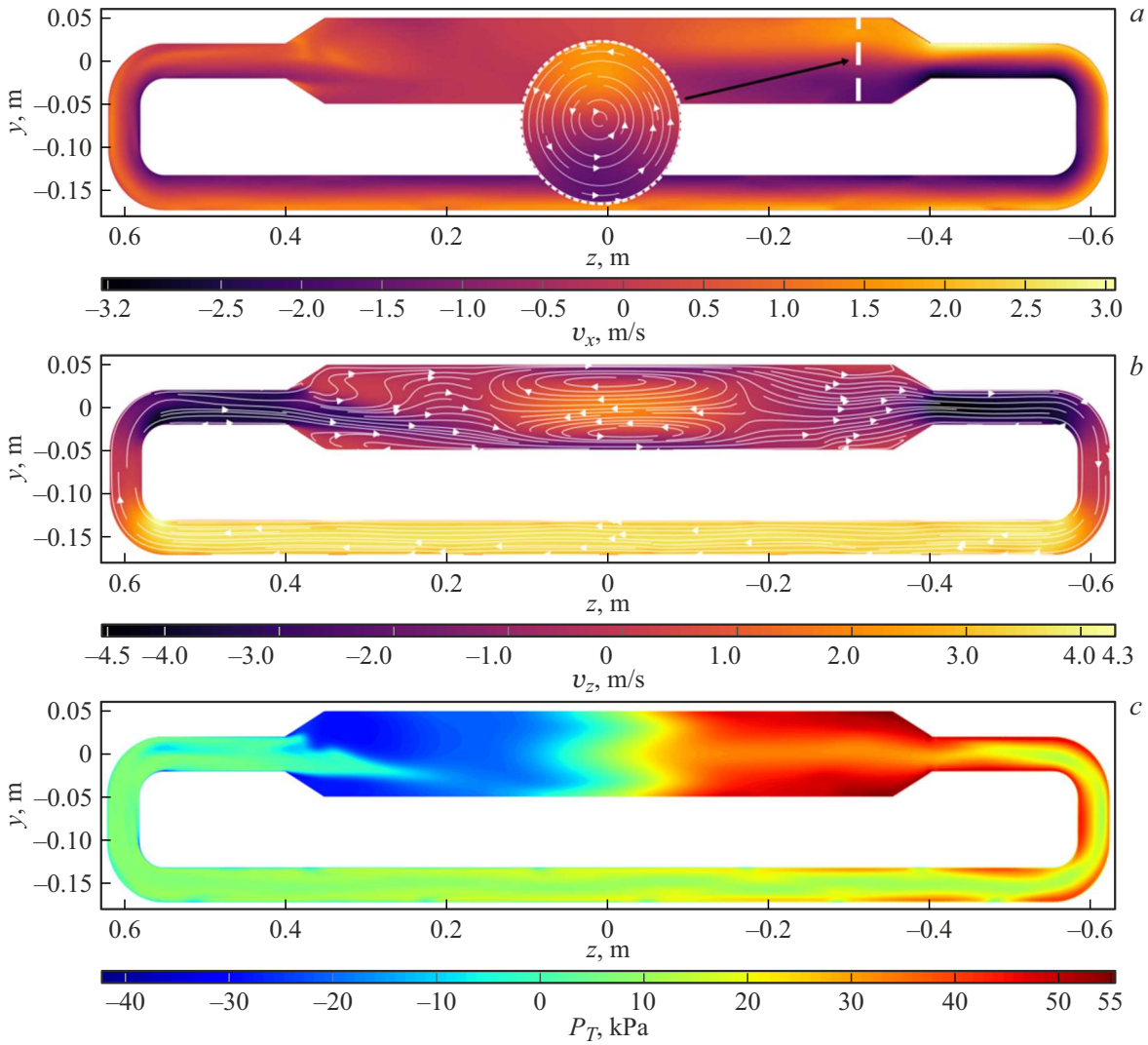

Figure 8. *a* — fields of velocity component v_x in the zy plane and xy plane (round inset); *b* — fields of velocity component v_z; *c* — fields of pressure P_T in the zy plane at $\gamma = 7.5 \cdot 10^{-3}$

the diffuse has a little slanted form (Figure 5, *b*), and non-zero values of v_x occur in the left-hand part of the main channel (Figure 5, *a*). Significant differential pressure is observed (Figure 5, *c*), and the main channel outlet pressure is much more uniformly distributed than the inlet pressure, which is also related to the interaction between the main and reverse flows, and probably with the bend section passed by the flow before entry into the main channel. On the contrary, in the case when $\gamma = 1$, the rotating flow, which has a well-defined structure, prevails over the transit flow, which is indicated by high values of v_x at the main channel walls (near 30 m/s) (Figure 6, *a*). Due to strong rotation in the center of the channel, two low pressure zone are formed on both sides of the RMF inductor (Figure 6, *a*), in which the fluid is drawn from the closing channel. Decrease in the differential pressure between the main channel inlet and outlet (Figure 6, *c*) leads to longitudinal flow degeneracy, moreover, pressure along the channel walls is very high.

Figure 7 shows dependences of the section average differential total pressure $\langle P_T \rangle$ between the main channel inlet and outlet $\Delta\langle P_T \rangle$, and of flow rate Q on γ.

$\langle P_T \rangle$ was assumed to be the average pressure over a surface formed by the xy plane section in domains marked with dashed lines (Figure 7, *a*). The results show that application of RMF with a small (compared with TMF) force parameter to the TMF-induced axial flow provides an increase in $\Delta\langle P_T \rangle$ (Figure 7, *b*). However, this effect is observed in a comparatively small range of values $\gamma \in [5 \cdot 10^{-3}, 10^{-2}]$. As γ grows, $\Delta\langle P_T \rangle$ starts decreasing rapidly down to near-zero values. This means that the flow changes to a condition where the rotating flow component prevails over the transit flow component, i.e. the flow almost completely transforms into rotating flow localized in the main channel (Figure 6, *a*, *b*). To explain this effect, consider in more detail the cases when $\gamma = 7.5 \cdot 10^{-3}$ (γ within the specified range) (Figure 8) and $\gamma = 1.5 \cdot 10^{-2}$

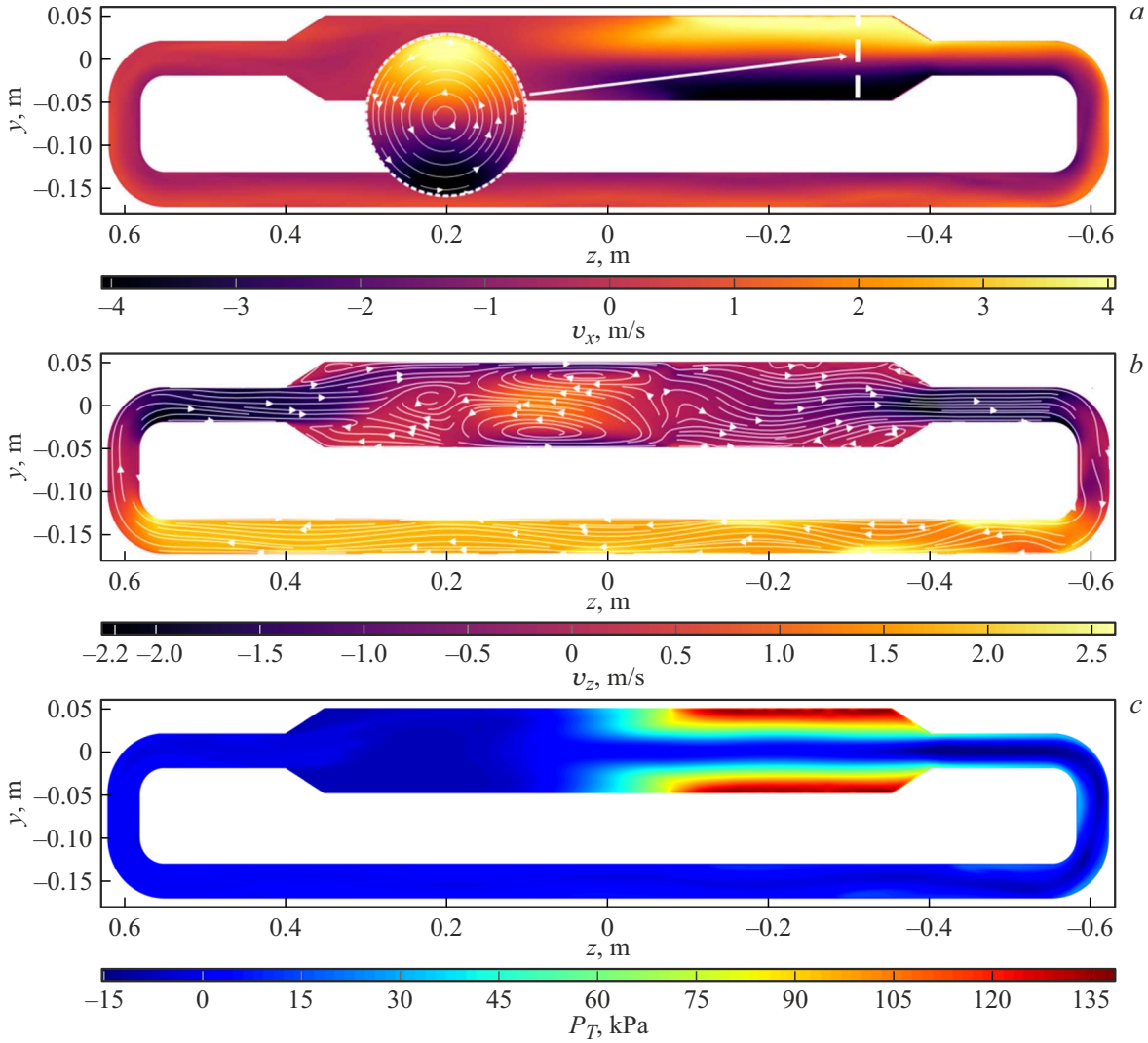

Figure 9. *a* — fields of velocity component v_x in the zy plane and xy plane (round inset); *b* — fields of velocity component v_z; *c* — fields of P_T in the zy plane at $\gamma = 1.5 \cdot 10^{-2}$.

(γ higher than that at the right-hand boundary of the range) (Figure 9).

Figure 8, *a* shows the joint action of TMF and RMF when v_x is non-zero almost throughout the channel. When the flow moves in the closing channel, its v_x gradually decreases with distance from the swirling zone. As the RMF intensity increases, the maximum pressure is concentrated at outer walls of the right-hand half of the main channel — where v_x is maximum. While a low pressure zone (a band in the center of the right-hand half of the main channel) is created in the center of the channel, due to a relatively small axial velocity component v_z and, accordingly, small flow in the closing channel. As γ further increases, these effects are obviously intensified. Figure 9, *a* shows that RMF-induced rotation presses the flow against the main channel walls. Maximum P_T is also there (Figure 9, *c*), which hinders the flow through the reducer, thus, the axial velocity component decreases (Figure 9, *b*), and, as a result, the flow loses its swirl almost in the very beginning of the closing channel.

The effect of TMF and RMF with different values of the corresponding force parameters on the flow is illustrated by the time dependence curves of (Figure 10): the kinetic force E_k, TMF-dependent poloidal flow component energy E_{pol}, RMF-dependent azimuthal flow component energy E_{az}. Ratios used for energy calculations are shown below. Ratios (8)–(10) are given in the cylindrical coordinate system; its origin coincides with the origin of the Cartesian system used above, and the link of the radial and azimuthal vector components to the corresponding Cartesian components is determined by the known equations. ρ was assumed as constant, therefore the problem addressed the energy related to ρ and domain volume V and, consequently, measured in $(\mathrm{m/s})^2$. V in this case is the volume of the main cylindrical channel, rather than of the whole domain.

$$E_{pol} = \frac{1}{V} \int_V (v_r^2 + v_z^2) dV, \tag{8}$$

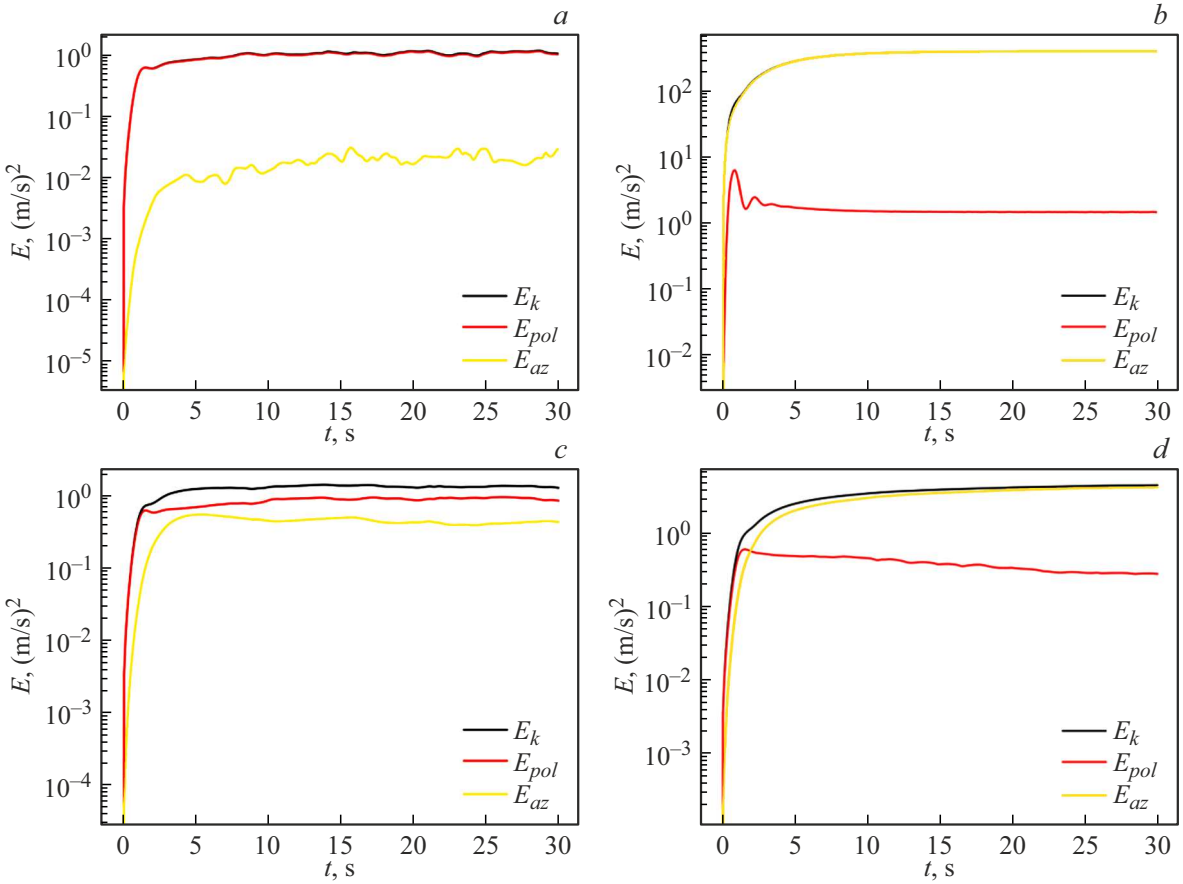

Figure 10. E_k, E_{pol} and E_{az} vs. time for force parameters: a — $\gamma = 10^{-3}$, b — $\gamma = 1$, c — $\gamma = 7.5 \cdot 10^{-3}$, d — $\gamma = 1.5 \cdot 10^{-2}$.

$$E_{az} = \frac{1}{V} \int_V v_\varphi^2 dV, \tag{9}$$

$$E_k = E_{pol} + E_{az}, \tag{10}$$

where v_r and v_φ are the radial and azimuthal velocity components in the cylindrical coordinate system, respectively.

Figures $10, a, b$ describe the minimum and maximum cases of γ. In the former case ($\gamma = 10^{-3}$), the poloidal flow component energy prevails, in the latter case ($\gamma = 1$), the azimuthal component prevails (Figure $10, b$). In both cases these energies almost coincide with the total kinetic energy of the flow, i.e. there is no any mutual influence between the transit and rotating flow components at such TMF and RMF force parameters. Other situation is observed in Figure $10, c, d$: when $\gamma = 7.5 \cdot 10^{-3}$, the effect of rotation on the flow is quite evident by the increased E_{az}, however, here TMF still plays the key role, which can be seen by quite close values of E_k and E_{pol}. With further increase to $\gamma = 1.5 \cdot 10^{-2}$, there is a drastic change in the situation: the main part of energy now consists of the rotation energy. Figure $9, d$ shows that E_{az} grows with time, and E_{pol} decreased accordingly. This is caused by the fact that the rotating flow zone in the main channel (zones near the main channel wall of the zone in Figure $9, a$) gradually expands to the left. Such expansion is probably attributed to the fact that fluid, passing via the closing channel, returns to the main channel and is drawn by RMF, while a part of fluid joins the rotation in the main channel, and another part continues its longitudinal motion throughout the channel.

Conclusion

Results of the numerical simulation of liquid metal flow in the closed-loop round cross-section channel under the joint action of TMF and RMF have shown that application of RMF to the TMF-induced flow can increase the differential pressure between the channel inlet and outlet (Figure $7, b$). Ratio of forces generated by TMF and RMF in liquid and distribution of the forces over the channel are important parameters affecting the flow behavior. As mentioned above, as γ grows, a differential pressure increase effect occurs. However, it can be observed in a small range of values up to $\gamma = 7.5 \cdot 10^{-3}$. With further growth of this parameter, rotation starts prevailing over the longitudinal flow, which decreases the differential pressure.

Within the numerical calculations, the maximum differential pressure was observed at $\gamma = 7.5 \cdot 10^{-3}$. At $\gamma < 5 \cdot 10^{-3}$, few or no changes in the hydrodynamic flow characteristics were observed. On the contrary, in the

cases when $\gamma > 10^{-2}$, RMF significantly contributed to the flow, suppressing the axial flow considerably. As soon as $\gamma = 5 \cdot 10^{-2}$ was reached, the axial flow in the channel actually stopped.

This is attributed to a number of reasons. RMF fluid swirling pressed the fluid against the channel walls, and the higher the RMF force parameter was the stronger the fluid was pressed, creating a high pressure zone at the walls, and a low pressure zone closer to the center. Due to the axial flow even at a low velocity, the rotating flow zone concentrated in the right-hand part of the main channel could expand to the left, involving an increasing volume into rotation and decelerating the axial flow. The higher the RMF force parameter was the faster it involved the fluid into rotation. Besides RMF, structural components, reducer and bends, were a serious negative factor for the axial flow. Note that reduction in the reducer area doesn't play any essential role in the absence of RMF (Figure 5, *b*), however, as it turned out in the course of numerical experiments where rotating fields were significant, it was the slanted reducer wall that considerably hindered the flow passage (Figure 6, *a*).

Increase in $\Delta\langle P_T \rangle$ can be achieved due to the fact that the transit flow is able to carry the rotation-defined angular momentum almost throughout the channel (Figure 8, *a*), if the angular momentum is relatively small and the magnitude of TMF is enough to overcome the rotation localization within the main channel as, for example, in Figure 6, *b*. Thus, the rotating flow is carried away by the axial flow from the main channel, presses the fluid against the channel wall at the main channel outlet and consequently increases the mean cross-section pressure and, accordingly, the differential pressure between the inlet and outlet.

Funding

The study was made in the framework of the government task, registration number of the theme 124012300246-9, and with financial assistance from the government of the Perm Krai under the scientific project „Development of electromagnetic pumps implementing transit and spiral flows of liquid metals in slit and cylindrical channels for metallurgical and nuclear industry devices“ (Agreement No. 26-08-08-35 dated January 29, 2024).

Conflict of interest

The authors declare no conflict of interest.

References

[1] M. Ni, J. Yang, J. Zhang. App. Mech. Rev., **1** (105), Art.N. AMR-24-1149 (2025). DOI: 10.1115/1.4067935
[2] A.M. Anisimov, I.V. Vitkovsky, M.M. Golovanov, I.R. Kirillov. Atomic Energy, **112** (6), 443 (2012). DOI: 10.1007/s10512-012-9581-y
[3] P.A. Davidson. *Introduction to Magnetohydrodynamics* (Cambridge University Press, Cambridge, 2001)
[4] A.I. Vol'dek. *Induktsionnye magnitogidrodinamicheskie mashiny s zhidkometallicheskim rabochim telom* (Energiya, L., 1970) (in Russian).
[5] S.Yu. Khriptchenko, E.Yu. Tonkov. ZhTF, **94** (10), 1729 (2024) (in Russian). DOI: 10.61011/JTF.2024.10.58868.181-24
[6] V.M. Arkhipov *Tekhnika raboty s natriem na AES* (Energoatomizdat, M., 1986) (in Russian)
[7] S. Dementjev, F. Groeschel, N. Jekabsons. Magnetohydrodynamics, **44** (3), 279 (2008). DOI: 10.22364/mhd.44.3.6
[8] I.V. Kolesnichenko, R.I. Khalilov. Vychislitelnaya mekhanika sploshnykh sred **15** (4), 495 (2023) (in Russian). DOI: 10.7242/1999-6691/2022.15.4.38
[9] H. Araseki, I.R. Kirillov, G.V. Preslitsky. Nuclear Engineering and Design, **243**, 111 (2012).
[10] K. Cukierski, B.G. Thomas. Metall. Mater. Trans. B, **3** (1), 94 (2008). DOI: 10.1007/s11663-007-9109-3
[11] I. Smolyanov, E. Shmakov, J. Vencels. Magnetohydrodynamics, **57** (6), 105 (2021). DOI: 10.22364/mhd.57.1.9
[12] I. Smolyanov, F. Sarapulov, F. Tarasov. Computers Mathematics with Applications, **78** (9), 3187 (2019). DOI: 10.1016/j.camwa.2019.05.015
[13] I.V. Kolesnichenko, I.Yu. Mitropolit, E. Golbraikh. Izvestiya RAN. Seriya fizicheskaya, **89** (7) (2025) (in Russian).
[14] I.V. Kolesnichenko, A.D. Mamykin, R.I. Khalilov. Vestnik Permskogo universiteta. Fizika, **4**, 45 (2022) (in Russian). DOI: 10.17072/1994-3598-2022-4-45-51
[15] I. Kolesnichenko, R. Okatev. Eur. Phys. J. Plus., **139**, 846 (2024). DOI: 10.1140/epjp/s13360-024-05629-7
[16] A. Cramer, J. Pal, G. Gerbeth. Phys. Fluids, **19**, 118109 (2007). DOI: 10.1063/1.2801407
[17] I. Grants, D. Raebiger, T. Vogt, S. Eckert, G. Gerbeth. Magnetohydrodynamics, **51**, 419 (2015). DOI: 10.22364/mhd.51.3.2
[18] S. Khripchenko. J. Eng. Phys. Thermophys., **95** (5), 1126 (2022). DOI: 10.1007/s10891-022-02577-w
[19] X. Zhang, C. Xu, C. Lei, T. Wang, H. Lin, H. Wu. Steel Res. Intern., **95** (1), 2300278 (2023). DOI: 10.1002/srin.202300278
[20] A.D. Mamykin. V.S. Ozernykh. Vychislitelnaya mekhanika sploshnykh sred **12** (1), 57 (2019) (in Russian). **17** (2), 247 (2024). DOI: 10.7242/1999-6691/2024.17.2.22
[21] J. Stiller, K. Koal, W.E. Nagel, J. Pal, A. Cramer. Eur. Phys. J. Special Topics, **220** (1), 111 (2013). DOI: 10.1140/epjst/e2013-01801-8
[22] I. Grants. G. Gerbeth. J. Cryst. Growth, **269** (2−4), 630 (2004). DOI: 10.1016/j.jcrysgro.2004.05.090
[23] F.R. Menter. AIAA J., **32** (8), 1598 (1994). DOI: 10.2514/3.12149
[24] F.R. Menter, M. Kuntz, R. Langtry. *Turbulence, Heat and Mass Transfer. Proceedings of the Fourth International Symposium on Turbulence, Heat and Mass Transfer* (Antalya, Turkey, 2003), v. 4, p. 625−632.
[25] R. Khalilov, I. Kolesnichenko. Magnetohydrodynamics, **51**, 95 (2015). DOI: 10.22364/mhd.51.1.10

Translated by E.Ilyinskaya